Journal of
Materials Chemistry A

Accepted Manuscript

This article can be cited before page numbers have been issued, to do this please use: D. Cardenas-Morcoso, R. Ifraemov, M. García-Tecedor, I. Liberman, S. Gimenez and I. Hod, *J. Mater. Chem. A*, 2019, DOI: 10.1039/C9TA01559K.

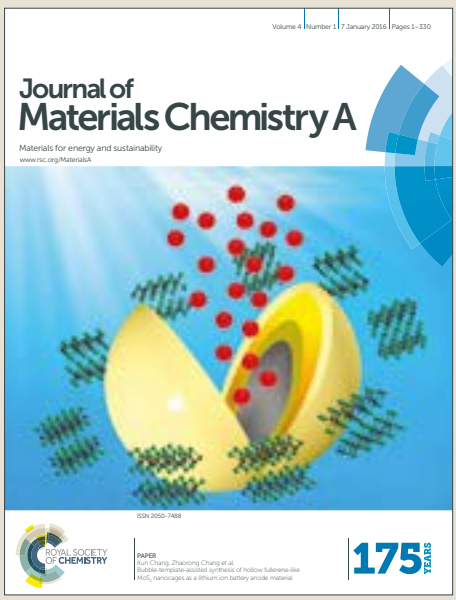

ROYAL SOCIETY OF CHEMISTRY

rsc.li/materials-a

View Article Online
DOI: 10.1039/C9TA01559K

ARTICLE

A Metal-Organic Framework Converted Catalyst that Boosts Photo-Electrochemical Water Splitting

Received 00th January 20xx,
Accepted 00th January 20xx

DOI: 10.1039/x0xx00000x

Drialys Cardenas-Morcoso, [†a] *Raya Ifraemov,* [†b] *Miguel García-Tecedor,*[a] *Itamar Liberman,* [b] *Sixto Gimenez,*[*a] *and Idan Hod,*[*b]

Realization of photo-electrochemical water splitting to generate H_2 alternative fuel requires the facilitation of the kinetically-sluggish oxygen evolution reaction (OER) occurring at the photoanode. To do so, there is a need to develop new methods to assemble suitable OER co-catalysts at the semiconductor-solution interface. Although Metal-Organic Frameworks (MOFs) are frequently used as precursor materials to synthesize high surface area, effective OER electrocatalysts, until now their utilization as co-catalysts in a working photo-electrochemical cell (PEC) remained underexplored. As a proof-of-concept, here we provide a simple route for modification of $BiVO_4$-based photoanodes with highly-active porous cobalt-oxide co-catalysts, converted from a cobalt-imidazolium MOF (ZIF-67). Photo-electrochemical and impedance spectroscopy analysis reveal that the co-catalyst significantly accelerates photoanodic OER (rather than serving as a surface passivation layer), and thus greatly improves the overall PEC performance. Hence, given the chemical flexibility of MOFs, this work provides a new tool-kit for designing efficient water splitting PECs.

Introduction

Photo-electrochemical cells (PECs) are considered to be one of the most promising and economically feasible future technologies for producing alternative energy sources and could be used to directly convert sunlight into chemical fuels, for example by splitting water to form molecular hydrogen, H_2.[1] The water splitting process consists of two half reactions, namely oxygen evolution reaction (OER) occurring at the anode and hydrogen evolution reaction (HER) at the cathode.[2] Due to its four-electron four-proton coupled reaction, OER kinetics is relatively sluggish, and thus it is generally considered to be the kinetic bottle-neck for the total water splitting process. Consequently, in order to achieve a highly efficient water splitting device, the performance of the OER half reaction at the anode must be improved.

TiO_2,[3] WO_3,[4] α-Fe_2O_3[5] and $BiVO_4$[6] are among the most studied semiconductors for photo-electrochemical OER, since they possess a suitable band gap and adequate energy level alignments for efficient solar light absorption and water oxidation respectively. However, drawbacks as low charge separation efficiency, high recombination rates and slow water oxidation kinetics, impedes the development of efficient PECs based on these materials. In that regard, a promising route for accelerating the kinetics of water oxidation at the photoanode's surface is through the utilization of a suitable co-catalyst capable of rapid delivery of photo-generated redox equivalents, from the semiconductor toward the electrolyte solution. Co-catalysts based on Ni, Co and Fe (metal oxides such as NiOOH,[7] FeOOH[8] and Co_3O_4,[9] as well as CoPi[10] and Prussian-blue based Co-hexacyanoferrate)[11] are widely studied and used, since they exhibit high electrocatalytic activity for OER coupled with good stability during harsh reaction conditions. Nevertheless, in order to achieve further enhancement in the performance of water oxidation PECs, there is still a need to develop new types of highly efficient OER co-catalysts. A key requirement for such improvement in catalytic activity is to design a highly porous catalyst-architecture, in order to expose large surface-concentrations of electrolyte-accessible catalytically-active OER sites.

Knowing that, we have realized the great potential of using Metal-Organic Frameworks (MOFs) based materials for designing a new family of OER co-catalysts. MOFs are a subclass of coordination polymers consisting of metal clusters and organic linkers.[12] They attracted widespread attention, due to their high surface area, porosity and tunable properties that can easily be controlled by a specific selection of metal nodes and organic linkers, resulting in diverse functionality. Therefore, they have been applied in fields such as gas storage and separation,[13, 14] chemical catalysis,[15-17] and sensing.[18, 19] Recently, increasing efforts have been put for utilizing MOFs in electrocatalytic applications.[20-26] However currently, the

[a] *Institute of Advanced Materials (INAM), Universitat Jaume I, 12071 Castelló, Spain*
[b] *Department of Chemistry and Ilse Katz Institute for Nanoscale Science and Technology, Ben-Gurion University of the Negev, Beer-Sheva 8410501, Israel.*
† *D.C.-M. and R.I. have equally contributed to this work*
Email - hodi@bgu.ac.il
Electronic Supplementary Information (ESI) available: [details of any supplementary information available should be included here]. See DOI: 10.1039/x0xx00000x

View Article Online
DOI: 10.1039/C9TA01559K

intrinsic low conductivity of most MOFs impedes their practical realization in electrochemical devices.[20, 27-29] To overcome this drawback, researchers have been using MOFs as a high surface area precursor material or templating agent to yield porous, conductive MOF-converted inorganic materials that possess unique electrocatalytic properties.[30-34] Hence, MOF-converted electrocatalysts contain all needed ingredients to construct highly efficient co-catalysts: high porosity, structural diversity and the desired intrinsic catalytic activity. Yet, despite the great progress in this field, to the best of our knowledge these MOF-converted materials have rarely been studied as co-catalysts in water splitting PECs.[35, 36]

Consequently, in this work we demonstrate that a great enhancement in the performance of a water splitting PEC could be achieved by a simple modification of the surface of a semiconducting photoanode with a MOF-derived, highly porous cobalt oxide (CoO_x) co-catalyst. As a proof-of-concept, we have chosen to focus our study on $BiVO_4$ based photoanodes. In order to achieve an homogenous co-catalyst coverage on top of the $BiVO_4$ surface, the sample is first modified with the well-known cobalt-imidazole-based ZIF-67 MOF. Thereafter, the deposited MOF was thermally converted into porous cobalt oxide via calcination in air. Due to the high surface area of the MOF precursor, the resulting porous co-catalyst exposes a large amount of catalytically-active water oxidation sites, thus allowing significant acceleration of water oxidation kinetics and overall improvement in the performance of the whole $BiVO_4$-based water splitting PEC.

Results and discussion

Scheme 1 schematically illustrates the growth of CoO_x based co-catalysts on $BiVO_4$ electrodes. First, ZIF-67 was synthesized according to a previously reported solvothermal route (see experimental section for detailed procedure). To enable a uniform growth and robust attachment of ZIF-67 on top of $BiVO_4$, a monolayer of Benzene-1,3,5-tricarboxylic acid (H_3BTC) was used to modify the surface of $BiVO_4$. Hereafter, ZIF-67 was grown by simply mixing cobalt nitrate and 2-methylimidazole in methanol at room temperature, yielding homogeneous coverage of MOF particles at the semiconductor's surface (termed $BiVO_4$-ZIF-67). We have fabricated five types of $BiVO_4$-ZIF-67 electrodes by setting the growth duration of the ZIF-67 on top of the $BiVO_4$ to 1, 4, 6, 8.5 and 12 hours, termed $BiVO_4$-ZIF-67_1h, $BiVO_4$-ZIF-67_4h, $BiVO_4$-ZIF-67_6h, $BiVO_4$-ZIF-67_8.5h and $BiVO_4$-ZIF-67_12h respectively. Thereafter, the as synthesized $BiVO_4$-ZIF-67 samples were calcinated at 400 °C for 3 hours in air, in order to convert the deposited MOF particles into CoO_x co-catalysts (termed $BiVO_4$-CoOx). We note that for comparison, all control $BiVO_4$ films in this work were also subject to the same calcination process at 400 °C for 3 hours in air (termed $BiVO_4$ (400 °C)).

The growth of crystalline ZIF-67 on the surface of the $BiVO_4$ electrodes was confirmed by X-ray diffraction (XRD) and Raman spectroscopy. The XRD pattern contains sharp peaks positioned at 2θ angles: 7.3, 10.3, 12.7, 14.6 and 17.9°, as shown in **Figure 1a** which corresponds to the ZIF-67. Upon calcination at 400 °C in air, the corresponding ZIF-67 XRD peaks disappear and new peaks appeared in at 38.4, 44.6, 65.0, and 78.1, which correspond to the (222), (400), (440) and (533) planes of spinel cobalt oxide.[37] Importantly, the peaks corresponding to $BiVO_4$ remain unaffected, meaning that the photoactive semiconductor preserves its crystallinity during the thermal treatment.

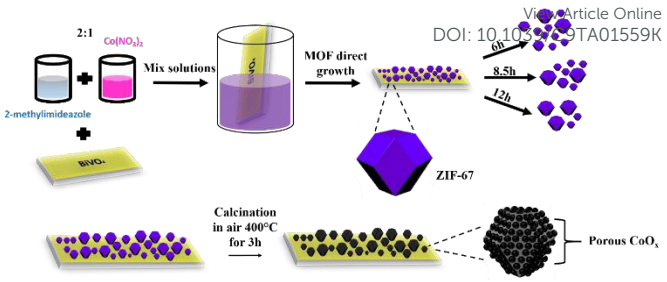

Scheme 1. Schematic illustration of the CoO_x co-catalyst growth procedure on $BiVO_4$ electrodes.

Moreover, characteristic Raman peaks of ZIF-67 were detected (**Figure 1b**).[30] In addition, the formation of cobalt oxide species after calcination was also confirmed by Raman spectroscopy, by clearly showing the appearance of additional peaks at 694 ,529 and 485 cm^{-1} corresponding to the vibrational modes of cobalt oxide and the disappearance of the peaks related to ZIF-67.[38] We note that for the $BiVO_4$-ZIF-67_6h sample an excitation laser beam of 633 nm was used (as opposed to 532 nm used for all other samples), since shorter excitation wavelengths caused significant light scattering from the $BiVO_4$ particles and thus prevented the detection of ZIF-67.

Scanning Electron Microscopy (SEM) images of $BiVO_4$-CoO_x electrodes reveal a homogeneous coverage of the crystalline $BiVO_4$ with nanoparticles of CoO_x having a size of a few tens of nanometers (**Figure 1c-d**). As seen in **Supporting Information, Table S1**, ICP-OES measurements confirm that ZIF-67 surface-loading is increased with longer growth duration (though no clear differences in the either CoO_x particle's size or density was observed by the SEM images in **Supporting Information, Figure S1**). Nevertheless, looking at lower SEM magnifications, one can detect the presence of a few dodecahedral particles (preserving the typical crystal morphology of the pristine ZIF-67 precursor[39]) with the average size of 0.5 µm on top of the $BiVO_4$ surface (**Supporting Information, Figure S2**). EDS elemental mapping analysis of the samples was performed using Scanning Transmission Electron Microscopy (STEM), revealing that the deposited particles on the $BiVO_4$ surface nanoparticles are indeed composed of cobalt oxide (**Figure 1e**). In order to confirm that the origin of the CoO_x nanoparticles is indeed the grown ZIF-67 precursor, SEM images were taken for both $BiVO_4$-ZIF-67_6h and a control $BiVO_4$ sample immersed only in the MOF's cobalt precursor, $Co(NO_3)_2$ for 6 hours, without 2-methylimidazole ligands (termed $BiVO_4$-$Co(NO_3)_2$_6h). For $BiVO_4$-ZIF-67_6h sample, the SEM images and EDS characterization (**Supporting Information, Figure S3a-c**) revealed a uniform coverage of CoO_x nanoparticles on the surface of the $BiVO_4$ particles, while for the $BiVO_4$-$Co(NO_3)_2$_6h

View Article Online
DOI: 10.1039/C9TA01559K

the $BiVO_4$ particles remained unmodified (**Supporting Information, Figure S3d-f**).

Additionally, in order to further confirm the conversion of ZIF-67 into highly porous CoO_x, ZIF-67 was synthesized in a powder form, thus enabling us to characterize the structural

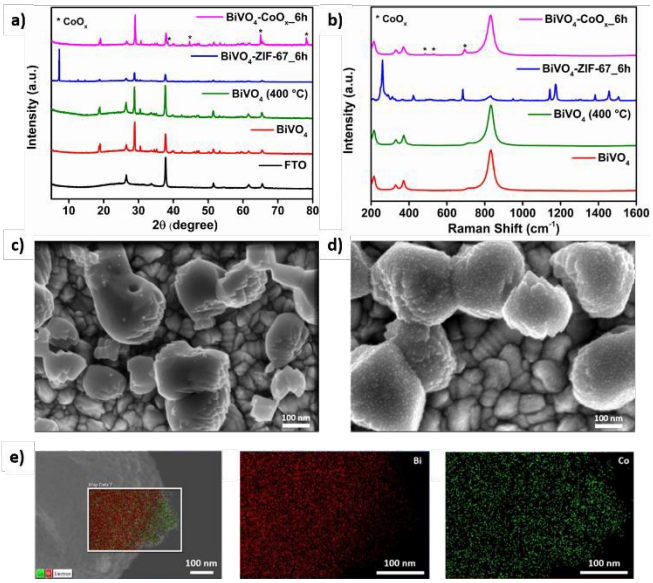

Figure 1. a) XRD patterns and b) Raman spectra of the bare $BiVO_4$ (red curve), $BiVO_4$ (400 °C) (green curve), $BiVO_4$-ZIF-67_6h (blue curve) and $BiVO_4$-CoO_x_6h (pink curve). The Raman spectra for the $BiVO_4$-ZIF-67_6h sample was obtained using a 633 nm excitation laser beam, while for all other samples 532 nm excitation was used. (we note that the Raman laser does not penetrate through the whole sample and thus no FTO related peaks are observed). c) SEM image of $BiVO_4$ film, d) SEM image of $BiVO_4$-CoO_x_6h film. e) Scanning Transmission Electron Microscopy (STEM) based EDS elemental mapping of $BiVO_4$-CoO_x_6h.

and surface area changes resulting from the MOF calcination in air. As can be seen in **Supporting Information, Figure S4**, PXRD of the calcinated ZIF-67 reveal the typical crystalline structure of cubic-shaped Co_3O_4. Transmission electron microscopy (TEM) images clearly show the porous, dodecahedral particles formed during the ZIF-67 calcination in air appears (**Supporting Information, Figure S5a**). Selected area electron diffraction (SAED) was performed to determine whether the calcinated ZIF-67 product is a crystalline Co_3O_4. The resulting diffraction rings are indeed associated with the (111), (220), (311), (400), (422), (511) and (440) crystal planes of cubic Co_3O_4 (JCPDS 42-1467) (**Supporting Information, Figure S5b**). N_2 isotherm of the ZIF-67 converted CoO_x show a BET surface area of 63 m^2/gr, thus confirming that the resulting $BiVO_4$-mounted co-catalysts are indeed highly porous and expose high density of electrolyte-accessible catalytically-active sites (**Supporting Information, Figure S6**).

Surface characterization of the $BiVO_4$-ZIF-67_6h and $BiVO_4$-CoO_x_6h films was carried out by X-ray photoelectron spectroscopy (XPS). The global XPS spectra of the films (**Supporting Information, Figure S7a and S8a**) show the characteristic split signal corresponding to the Bi $4f_{5/2}$ and Bi $5f_{7/2}$ orbitals of Bi^{3+} state in $BiVO_4$, the V 2p and O 1s signals corresponding to V^{5+} and O^{2-} ions respectively and the characteristic Zr 3d and Zr 3p signals. Since the amount of Zr is at the detection limit of the equipment, the ratios between the Zr $3p_{1/2}$ and Zr $3p_{3/2}$ areas, could not be properly quantified with this technique. The presence of Sn in the XPS spectra arises from the underlying FTO substrate, which is exposed at some locations due to the porous nature of the specimens.

The $BiVO_4$-ZIF-67_6h films show a N1s signal with 2 distinct

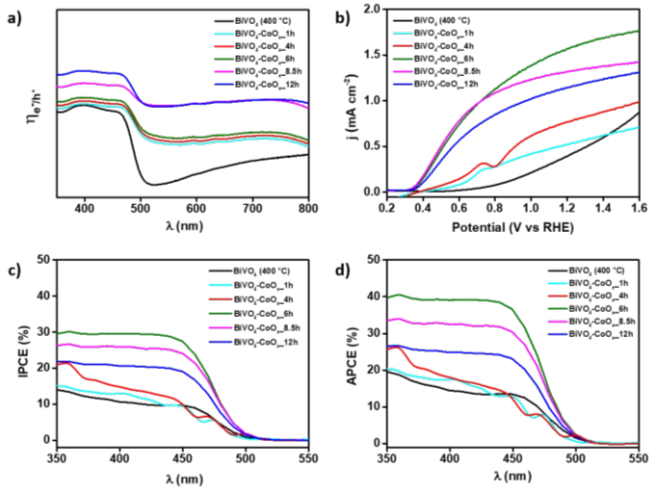

Figure 2. a) UV-Vis absorption spectra of $BiVO_4$ (400 °C) (control) and $BiVO_4$ with different loading of the MOF-converted CoO_x catalyst, b) j-V curves obtained with cyclic voltammetry c) IPCE and d) APCE spectra obtained from IPCE and absorbance measurements at 1.23 V vs RHE.

peaks at binding energies of 398.8 and 399.9 eV (**Supporting Information, Figure S8b**). The main peak located at 398.8 eV corresponds to N coordinated with Co^{2+} ions in ZIF-67, while the small peak at 399.9 eV corresponds to uncoordinated 2-methylimidazole (ZIF-67 surface defects).[30] The signal for Co 2p exhibits a single peak at 780.7 eV that corresponds to $Co2p_{3/2}$ and its satellite at 784.8 eV, attributed a Co-N species within the ZIF-67 MOF (**Supporting Information, Figure S8c**).[40]

For the calcinated $BiVO_4$-CoO_x_6h film, signals of N1s were not detected, which confirms the full conversion of ZIF-67 into porous CoO_x. As can be seen in **Figure S9**, the Co 2p signal of $BiVO_4$-CoO_x_6h exhibit 2 distinct peaks at binding energies of 783.1 and 780.6 eV, which are attributed to the co-existence of non-stoichiometric (CoO_x) and stoichiometric (Co_3O_4) cobalt oxide phases respectively at the surface of the electrode.[41, 42]

The optical properties of the control $BiVO_4$ (400 °C) films and upon deposition of different catalyst loadings (corresponding to 1, 4, 6, 8.5 and 12 hours) are showed in **Figure 2a**. $BiVO_4$ supra bandgap absorption takes place at wavelengths below 550 nm, in good agreement with previous reports.[43] It has been reported that nanostructured $BiVO_4$ prepared by electrochemical deposition induce light scattering,[44] as evidenced by the measured absorbance at wavelengths >550 nm. It is clear that the deposition of the MOF-converted co-catalyst significantly enhances both light scattering and $BiVO_4$ supra bandgap absorption, which is beneficial for light harvesting and solar energy conversion.

The photoelectrochemical behaviour of these films for water oxidation is summarized in **Figure 2b-d**. The photocurrent onset for the control sample takes place at 0.6 V vs RHE, which

is around 300 mV more anodic than the flatband potential (vide infra). Moreover, the characteristic s-shape of the j-V curve is a clear indication of excessive surface losses,[45, 46] most probably related to surface recombination.[47, 48] Samples with 1 h and 4 h growth time showed slightly enhanced performance compared to the control, but also exhibiting high surface losses and a redox wave around 0.6 - 0.7 V vs RHE, which could originate from non-oxidized Co species, and may suggest incomplete MOF conversion into an active CoO_x co-catalyst. A totally distinct behaviour is observed upon deposition of the MOF-converted co-catalyst after 6 h, 8.5 h and 12 h growth time, with photocurrent onsets very close to the flatband potential for $BiVO_4$ (vide infra) and a significant reduction of surface losses, as evidenced by the shape of the j-V curve. The highest photocurrents are obtained for the 6 hours CoO_x growth duration, clearly indicating that optical absorbance is not the main reason behind the increase of performance. Incident Photon to Current Efficiency (IPCE) was evaluated to understand the spectral signature of the photocurrent, (**Figure 2c**). The photocurrent onset at λ = 525 nm clearly indicates that the absorbance measured at wavelengths >550 nm is not productive for photoinduced charge extraction. Additionally, the deposition of the MOF-converted co-catalyst does not modify the photocurrent onset, corroborating that the changes in the optical properties induced by the co-catalyst are not relevant for the operation of the photoanode. The total photocurrent was calculated from integration of IPCE with the solar spectrum, and the values are included in **Supporting Information, Table S2** showing perfect agreement with those obtained by voltammetry measurements (**Figure 2b**). The Absorbed Photon to Current Efficiency (APCE) was also estimated by integration of the absorptance spectra of the films with the IPCE (**Figure 2d**). $BiVO_4$-CoO_x_6h electrodes exhibit the highest Internal Quantum Efficiencies, confirming that 6 hours deposition time leads to the best photoelectrochemical performance. As can be seen in **Supporting Information, Figure S10**, the photoelectrochemical properties of the $BiVO_4$-$Co(NO_3)_2$_6h samples are very similar to those of $BiVO_4$ (400 °C control) films, thus confirming the fact that the ZIF-67 converted co-catalysts are the one responsible for the catalytic enhancement.

Figure 3a shows the j-V curves of the control and the $BiVO_4$-CoO_x samples under illumination with and without the presence of presence of a hole scavenger (0.1M Na_2SO_3). In the presence of the hole scavenger, the photocurrent onset is a good approximation of the flatband potential of the $BiVO_4$ photoabsorber.[49] The obtained value of ~0.3 V vs RHE is slightly more anodic than usually reported values.[43, 44, 50] Furthermore, from these measurements, the charge separation efficiency (η_{cs}) and the charge injection efficiency (η_{cat}) could be estimated (**Figure 3b**), clearly indicating that the MOF-converted co-catalyst is responsible for a remarkable increase of the charge injection efficiency of the photoanode, up to voltages close to 1.8 V vs RHE, where the high applied electric field vanishes surface recombination. Conversely, the charge separation efficiency is not affected by the presence of the MOF-converted catalyst and is controlled by the bulk of $BiVO_4$.

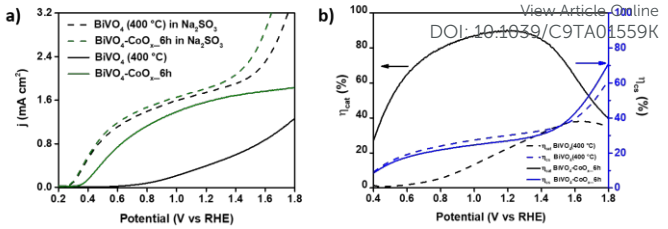

Figure 3. a) j-V curves of $BiVO_4$ (400 °C) and $BiVO_4$-CoO_x_6h electrodes with and without a sacrificial hole scavenger (0.1M Na_2SO_3) in the electrolyte solution. b) Charge injection (black lines) and charge separation (blue lines) efficiencies of $BiVO_4$ (400 °C) (dashed lines) and $BiVO_4$-CoO_x_6h (solid lines) electrodes.

Further mechanistic insights were extracted from impedance spectroscopy measurements in the dark and under illumination for both the control and the best performing $BiVO_4$-CoO_x electrode. The Nyquist impedance plots showed the presence of only one arc and consequently, a simple Randles' electrical equivalent circuit was employed to fit the experimental data (see **Supporting Information, Figure S11**). This model includes a series resistance (R_s) accounting for the resistance of the solution and the contacts, the charge transfer resistance from the electrode to the electrolyte (R_{ct}) and a capacitance (C). Although this selected model oversimplifies the real operation of these complex electrodes, (e.g. direct charge transfer from the FTO to the solution is not considered here, and the MOF-converted catalyst is not explicitly considered in the analysis), the extracted results still provide useful information on the kinetics of the processes taking place and on the charge storage modes of this system. In all cases, the series resistance R_s spans between 20 - 60 $\Omega \cdot cm^2$ (**Supporting Information, Figure S12**). On the other hand, the charge transfer resistance at the $BiVO_4$/solution interface (R_{ct}) governs the water oxidation kinetics and decreases both upon addition of the MOF-converted catalyst and under illumination (**Figure 4a**). In the dark, this resistance is not expected to change upon addition of the MOF-converted catalyst, since all minority carriers from $BiVO_4$ injected into the solution must be photogenerated. However, the observed decrease of this resistance in our experimental results can be explained by the enhanced direct dark water oxidation electrocatalysis from the FTO/CoO_x substrate (see **Supporting Information, Figure S13**, SEM image of FTO/CoO_x sites). Under illumination, a significant decrease of R_{ct} takes place for both the control and $BiVO_4$-CoO_x electrodes. The control sample shows a decrease of charge-transfer resistance with applied anodic bias, which is attributed to the enhanced suppression of surface recombination in these

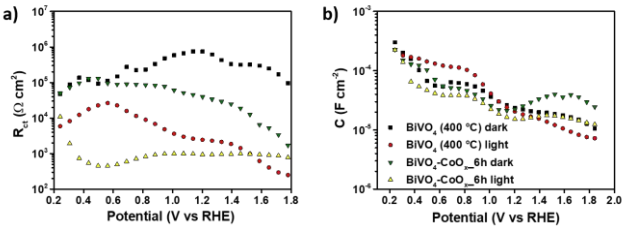

Figure 4. Parameters extracted from fitting the impedance spectroscopy data with the equivalent circuit model shown at Supporting Information, Figure S7. (a) Charge transfer resistance (Rct) (b) Capacitance (C).

View Article Online
DOI: 10.1039/C9TA01559K

conditions.[47, 48] However, in $BiVO_4$-CoO_x electrodes, a low R_{ct} value remains practically constant over a wide range of applied potentials (0.7V – 1.6V vs RHE), suggesting for fast water oxidation kinetics arising due to the catalytic activity of the CoO_x co-catalyst. It is interesting to note that this behaviour resembles the charge separation efficiency (η_{cs}) plot in **Figure 3b**, which also reaches a constant maximum value at a similar potential range. We note that the lower R_{ct} obtained for the control $BiVO_4$ (400 °C) sample at potentials more anodic than 1.6 V vs RHE is consistent with the higher slope of the j-V curve at these potentials, as can clearly be observed in Figure 2b.The obtained capacitances (**Figure 4b**) do not significantly change for the different conditions tested and exhibit the expected behaviour for an n-type semiconductor (decreasing at more anodic applied potentials), although the complexity of the films does not allow obtaining a reliable Mott-Schottky behaviour. Indeed, the capacitance at the most negative potentials seems to be controlled by the FTO.[51] The fact that for all samples we observe similar potential dependent capacitance at the $BiVO_4$/electrolyte interface, serves as a good indication that the deposited MOF-converted co-catalyst does not affect the

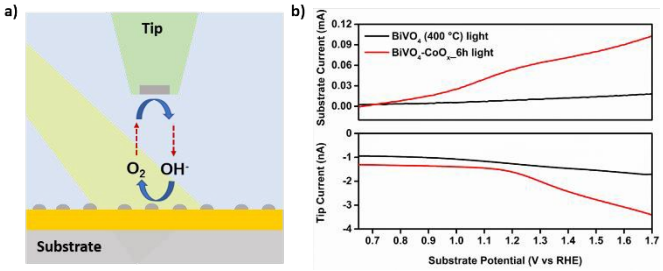

Figure 5. a) Schematic illustration of an SECM-based substrate-generation tip-collection experiment for direct detection of photoelectrochemical O_2 evolution. b) Substrate-generation tip-collection LSV curves of $BiVO_4$ (400 °C) (black lines) and $BiVO_4$-CoO_x_6h (red lines).

energy-band alignment of the $BiVO_4$ electrodes, as showed in a recent study[52] or passivate surface states[53] but rather acts as a true electrocatalyst. The total resistance extracted from impedance spectroscopy ($R_{total} = R_s + R_{ct}$) matched reasonably well that obtained by derivation of the j-V curve, $R_{total} = (dj/dV)^{-1}$ (see **Supporting Information, Figure S14**), validating the impedance analysis. Additionally, the j-V curves obtained from cyclic voltammetry before and after the impedance measurements were also in good correspondence with the j-V curves from impedance spectroscopy (**Supporting Information, Figure S15**).

Next, we were interested in understanding whether the enhanced photoelectrochemical activity of $BiVO_4$-CoO_x_6h is directly correlated with accelerated catalytic oxygen evolution. As illustrated in **Figure 5a**, to do so, we have used a Scanning Electrochemical Microscope (SECM) setup to perform a substrate ($BiVO_4$-CoO_x_6h or control $BiVO_4$)-generation tip (10µm Pt-based ultramicroelectrode)-collection under illumination (using a 405nm LED with calibrated illumination intensity of 2mW/cm^2). First, the Pt tip was brought into close proximity of the photoanodes surface (10 µm, see approach curves in **Supporting Information, Figure S16**). Hereafter, light illumination was turned on and the substrate potential was scanned anodically to photoelectrochemically generate O_2. At the same time, direct O_2 detection was achieved by fixing the tip potential at 0.1V vs RHE to effectively reduce substrate-evolved O_2 at a mass-transport limited rate. As can be seen in **Figure 5b**, oxidative substrate photocurrent is followed by reductive tip current, thus providing a direct confirmation for the photo-electrocatalytic O_2 generation. Additionally, further evidence for the enhanced water oxidation kinetics of $BiVO_4$-CoO_x_6h compared to the control $BiVO_4$ is given by its significantly higher O_2 detection current measured at the tip.

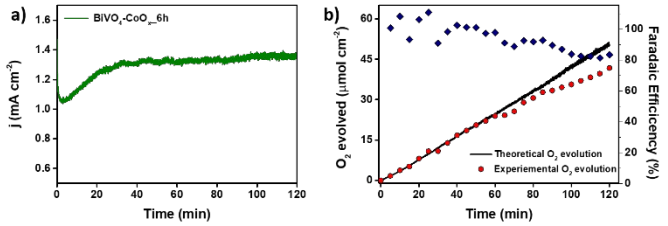

Figure 6. (a) Chronoamperometric measurement at 1.23 V vs RHE in a $BiVO_4$-CoO_x_6h electrode, showing the first two hours in which gas chromatography measures were performed. (b) O_2 evolution detection and faradaic efficiency extracted by gas chromatography.

The stability of the best performing photoanode ($BiVO_4$-CoO_x_6h) was also evaluated through chronoamperometric measurements. During the first two hours of catalysis, the photocurrent remains practically constant, after a 20 min stabilization time (**Figure 6a**). Furthermore, connecting a gas chromatograph to the photoelectrochemical cell, we could confirm the oxygen evolution takes place with a faradaic efficiency of ~100%. The scattering of the Faradaic efficiency during this period is due to flux control issues during the manual sampling process (**Figure 6b**).

After 2 hours of operation, the same electrode was subject to additional, long chronoamperometric test (24 hours) (**see Supporting Information, Figure S17**). At this point, one can see a rapid decline of the measured photocurrent occurring during the first 2 hours, significantly slowing down for the next 22 hours. Examination of post-mortem SEM micrographs and EDS analysis, (**Supporting Information, Figure S18**), suggests that the main factor for the performance loss can be ascribed to the degradation of both $BiVO_4$ and the MOF-converted co-catalyst, as evidenced by the decrease of Bi, V and Co concentrations (we note that this information does not provide any support for a possible role of the MOF-converted catalyst as a passivation layer)**.** This conclusion is also supported by post-catalysis ICP-MS and XPS quantitative analysis of the supernatant electrolyte solution and the aged electrode surface respectively, which shows the presence of significant quantities of Co, Bi and V in the electrolyte solution and the decrease of the presence of these elements on the electrode surface (See **Supporting Information, Tables S3 and S4**). In addition, the reduced activity of the photoanode over time may also be ascribed to a chemical alteration of the cobalt oxide-based co-catalyst during photo-electrochemical water oxidation. As can be seen in **Supporting Information Figure S19**, Co 2p XPS signal analysis reveal that as

opposed to the pristine films, the surface of the co-catalyst at the aged electrode contains only a stochiometric Co_3O_4 phase (as a result of the harsh oxidizing environment during catalytic operation).

Conclusions

In this work we demonstrate that a porous MOF-converted compound could be utilized as a highly efficient water oxidation co-catalyst in a photo-electrochemical cell. As a proof-of-concept, we have modified a $BiVO_4$-based photoanode with the well-known cobalt-based ZIF-67 MOF. Upon thermal treatment in air, the ZIF-67 was converted into highly porous CoO_x nanoparticles. Detailed photo-electrochemical characterization of the co-catalyst modified photoanodes, reveal a substantial improvement in the catalytic performance compared to the bare $BiVO_4$ electrode (~4-times higher photocurrents coupled with a 300 mVs cathodic shift in catalytic onset potential). Furthermore, measurements with a fast hole scavenger as well as electrochemical impedance spectroscopy analysis point to the fact that the MOF-converted co-catalysts significantly accelerate the kinetics of water oxidation, rather than serving as a surface passivation layer. Hence, we believe that these results will pave the way for the future design of highly efficient photo-electrochemical cells, to be used in a variety of energy related applications.

Acknowledgements

S.G thanks the support of the Spanish Ministerio de Ciencia, Innovación y Universidades through the project ENE2017-85087-C3-1-R. I.H thank the support of the Israel Science Foundation (ISF) (grant No. 306/18), and the Ilse Katz Institute for Nanoscale Science and Technology for the technical support in material characterization

Conflicts of interest

There are no conflicts to declare.

Author contribution

† D.C.-M. and R.I. have equally contributed to this work

References

1. Z. S. Li, W. J. Luo, M. L. Zhang, J. Y. Feng and Z. G. Zou, *Energy Environ. Sci.*, 2013, **6**, 347-370.
2. M. G. Walter, E. L. Warren, J. R. McKone, S. W. Boettcher, Q. Mi, E. A. Santori and N. S. Lewis, *Chem. Rev.*, 2010, **110**, 6446-6473.
3. M. Ge, J. Cai, J. Iocozzia, C. Cao, J. Huang, X. Zhang, J. Shen, S. Wang, S. Zhang, K.-Q. Zhang, Y. Lai and Z. Lin, *Int. J. Hydrogen Energy*, 2017, **42**, 8418-8449.
4. P. Dong, G. Hou, X. Xi, R. Shao and F. Dong, *Environ. Sci. Nano*, 2017, **4**, 539-557.
5. K. Sivula, F. Le Formal and M. Graetzel, *ChemSusChem*, 2011, **4**, 432-449.
6. T. W. Kim and K.-S. Choi, *Science*, 2014, **343**, 990-994.
7. L. Trotochaud, S. L. Young, J. K. Ranney and S. W. Boettcher, *J. Am. Chem. Soc.*, 2014, **136**, 6744-6753.
8. D. Friebel, M. W. Louie, M. Bajdich, K. E. Sanwald, Y. Cai, A. M. Wise, M.-J. Cheng, D. Sokaras, T.-C. Weng, R. Alonso-Mori, R. C. Davis, J. R. Bargar, J. K. Norskov, A. Nilsson and A. T. Bell, *J. Am. Chem. Soc.*, 2015, **137**, 1305-1313.
9. F. Jiao and H. Frei, *Angew. Chem. Int. Ed.*, 2009, **48**, 1841-1844.
10. M. W. Kanan and D. G. Nocera, *Science*, 2008, **321**, 1072-1075.
11. S. Pintado, S. Goberna-Ferron, E. C. Escudero-Adan and J. Ramon Galan-Mascaros, *J. Am. Chem. Soc.*, 2013, **135**, 13270-13273.
12. H. Furukawa, K. E. Cordova, M. O'Keeffe and O. M. Yaghi, *Science*, 2013, **341**, 1230444.
13. B. J. Furlong and M. J. Katz, *J. Am. Chem. Soc.*, 2017, **139**, 13280-13283.
14. J. L. C. Rowsell and O. M. Yaghi, *Angew. Chem. Int. Edit.*, 2005, **44**, 4670-4679.
15. J. Lee, O. K. Farha, J. Roberts, K. A. Scheidt, S. T. Nguyen and J. T. Hupp, *Chem. Soc. Rev.*, 2009, **38**, 1450-1459.
16. L. Zhu, X. Q. Liu, H. L. Jiang and L. B. Sun, *Chem. Rev.*, 2017, **117**, 8129-8176.
17. J. E. Mondloch, M. J. Katz, W. C. Isley, P. Ghosh, P. L. Liao, W. Bury, G. Wagner, M. G. Hall, J. B. DeCoste, G. W. Peterson, R. Q. Snurr, C. J. Cramer, J. T. Hupp and O. K. Farha, *Nat. Mater.*, 2015, **14**, 512-516.
18. L. E. Kreno, K. Leong, O. K. Farha, M. Allendorf, R. P. Van Duyne and J. T. Hupp, *Chem. Rev.*, 2012, **112**, 1105-1125.
19. M. G. Campbell, S. F. Liu, T. M. Swager and M. Dinca, *J. Am. Chem. Soc.*, 2015, **137**, 13780-13783.
20. I. Hod, M. D. Sampson, P. Deria, C. P. Kubiak, O. K. Farha and J. T. Hupp, *ACS. Catal.*, 2015, **5**, 6302-6309.
21. J. X. Liu and C. Woll, *Chem. Soc. Rev.*, 2017, **46**, 5730-5770.
22. P. M. Usov, B. Huffman, C. C. Epley, M. C. Kessinger, J. Zhu, W. A. Maza and A. J. Morris, *ACS. Appl. Mater. Inter.*, 2017, **9**, 33539-33543.
23. N. Kornienko, Y. B. Zhao, C. S. Kiley, C. H. Zhu, D. Kim, S. Lin, C. J. Chang, O. M. Yaghi and P. D. Yang, *J. Am. Chem. Soc.*, 2015, **137**, 14129-14135.
24. E. M. Miner, T. Fukushima, D. Sheberla, L. Sun, Y. Surendranath and M. Dinca, *Nat. Commun.*, 2016, **7**, 10942.
25. I. Hod, W. Bury, D. M. Karlin, P. Deria, C. W. Kung, M. J. Katz, M. So, B. Klahr, D. N. Jin, Y. W. Chung, T. W. Odom, O. K. Farha and J. T. Hupp, *Adv. Mater.*, 2014, **26**, 6295-6300.
26. I. Hod, W. Bury, D. M. Gardner, P. Deria, V. Roznyatovskiy, M. R. Wasielewski, O. K. Farha and J. T. Hupp, *J. Phys. Chem. Lett.*, 2015, **6**, 586-591.
27. I. Hod, O. K. Farha and J. T. Hupp, *Chem. Commun.*, 2016, **52**, 1705-1708.
28. S. Y. Lin, P. M. Usov and A. J. Morris, *Chem. Commun.*, 2018, **54**, 6965-6974.
29. R. Ifraemov, R. Shimoni, W. He, G. Peng and I. Hod, *J. Mater. Chem. A*, 2019, **7**, 3046-3053.
30. W. He, R. Ifraemov, A. Raslin and I. Hod, *Adv. Funct. Mater.*, 2018, **28**, 1707244.
31. X. H. Cao, C. L. Tan, M. Sindoro and H. Zhang, *Chem. Soc. Rev.*, 2017, **46**, 2660-2677.

View Article Online
DOI: 10.1039/C9TA01559K

32. S. Dang, Q. L. Zhu and Q. Xu, *Nat. Rev. Mater.*, 2018, **3**, 17075.
33. L. Oar-Arteta, T. Wezendonk, X. H. Sun, F. Kapteijn and J. Gascon, *Mat. Chem. Front.*, 2017, **1**, 1709-1745.
34. G. Yilmaz, K. M. Yam, C. Zhang, H. J. Fan and G. W. Ho, *Adv. Mater.*, 2017, **29,** 1606814.
35. W. Zhang, R. Li, X. Zhao, Z. Chen, A. W.-K. Law and K. Zhou, *ChemSusChem*, 2018, **11**, 2710-2716.
36. Z. Jiao, J. Zheng, C. Feng, Z. Wang, X. Wang, G. Lu and Y. Bi, *ChemSusChem*, 2016, **9**, 2824-2831.
37. L. T. Anh, A. K. Rai, T. V. Thi, J. Gim, S. Kim, V. Mathew and J. Kim, *J. Mater. Chem. A*, 2014, **2**, 6966-6975.
38. V. G. Hadjiev, M. N. Iliev and I. V. Vergilov, *J. Phys. C Solid State*, 1988, **21**, L199-L201.
39. G. H. Zhong, D. X. Liu and J. Y. Zhang, *J. Mater. Chem. A*, 2018, **6**, 1887-1899.
40. J. Qin, S. Wang and X. Wang, *Appl. Catal. B Environ.*, 2017, **209**, 476-482.
41. Y. S. Xia, H. X. Dai, H. Y. Jiang and L. Zhang, *Catal. Commun.*, 2010, **11**, 1171-1175.
42. C. V. Schenck, J. G. Dillard and J. W. Murray, *J. Colloid Interf. Sci.*, 1983, **95**, 398-409.
43. M. N. Shaddad, M. A. Ghanem, A. M. Al-Mayouf, S. Gimenez, J. Bisquert and I. Herraiz-Cardona, *ChemSusChem*, 2016, **9**, 2779-2783.
44. M. N. Shaddad, D. Cardenas-Morcoso, P. Arunachalam, M. García-Tecedor, M. A. Ghanem, J. Bisquert, A. Al-Mayouf and S. Gimenez, *J. Phys. Chem. C*, 2018, **122**, 11608-11615.
45. X. Shi, I. Herraiz-Cardona, L. Bertoluzzi, P. Lopez-Varo, J. Bisquert, J. H. Park and S. Gimenez, *Phys. Chem. Chem. Phys.*, 2016, **18**, 9255-9261.
46. L. Bertoluzzi, P. Lopez-Varo, J. A. Jimenez Tejada and J. Bisquert, *J. Mater. Chem. A*, 2016, **4**, 2873-2879.
47. C. Zachaus, F. F. Abdi, L. M. Peter and R. van de Krol, *Chem. Sci.*, 2017, **8**, 3712-3719.
48. M. Yimeng, K. Andreas, P. S. R., L. F. Florian and D. J. R., *Adv. Funct. Mater.*, 2016, **26**, 4951-4960.
49. S. Gimenez and J. Bisquert, *Photoelectrochemical Solar Fuel Production: From Basic Principles to Advanced Devices*, Springer Customer Service Center Gmbh, 2018.
50. B. J. Trzesniewski, I. A. Digdaya, T. Nagaki, S. Ravishankar, I. Herraiz-Cardona, D. A. Vermaas, A. Longo, S. Gimenez and W. A. Smith, *Energy Environ. Sci.*, 2017, **10**, 1517-1529.
51. F. Simone Hegner, I. Herraiz-Cardona, D. Cardenas-Morcoso, N. Lopez, J.-R. Galan-Mascaros and S. Gimenez, *ACS. Appl. Mater. Interfaces*, 2017, **9**, 37671-37681.
52. Y. Hermans, S. Murcia-López, A. Klein, R. van de Krol, T. Andreu, J. R. Morante, T. Toupance and W. Jaegermann, *Phys. Chem. Chem. Phys.*, 2019, **21**, 5086-5096.
53. B. Lamm, B. J. Trześniewski, H. Döscher, W. A. Smith and M. Stefik, *ACS Energy Lett.*, 2018, **3**, 112-124.

View Article Online
DOI: 10.1039/C9TA01559K

Table of contents entry:

We show that a MOF-converted compound can act as highly active co-catalyst in a water splitting photo-electrochemical cell.